Microstructure Characteristics and Comparative Analysis of Constitutive Models for Flow Stress Prediction of Inconel 718 Alloy

Gauri Mahalle ⑥, *Nitin Kotkunde, Amit Kumar Gupta, R. Sujith, Swadesh Kumar Singh, and Y.C. Lin*

An accurate constitutive model is essential for analyzing deformation behavior of material and reliable numerical simulations in metal forming processes. In this study, hot tensile tests of Inconel 718 alloy have been conducted over a wide range of temperatures (300-973 K at an interval of 100 K), strains (0.01-0.3 at an interval of 0.01) and quasi-static strain rates (0.0001, 0.001, 0.01 s^{-1}). Flow stress behavior is significantly affected by test temperatures and strain rates. Microstructure characteristics of deformed test specimens have been examined using scanning electron microscope and electron backscatter diffraction (EBSD). The fractography study revealed that fracture is mix-mode type, i.e., ductile and brittle. Subsequently, EBSD analysis shown that dynamic recrystallization mechanism is more pronounced at a higher temperature. Furthermore, four constitutive models, namely modified Cowper–Symonds, modified Johnson Cook, modified Zerillie-Armstrong and integrated Johnson Cook–Zerillie-Armstrong (JC-ZA) models have been investigated for flow stress prediction. Capability of models has been evaluated based on the correlation coefficient (R), average absolute error (Δ) and its standard deviation (δ). Accurate prediction of flow stress behavior is found by integrated JC-ZA model with R = 0.9873, Δ = 2.44 and δ = 4.08%.

1. Introduction

High-strength Inconel 718 alloy is a special grade of precipitation-hardenable Ni-Fe-Cr-based superalloys with higher concentration (by wt.%) of nickel (51-61%), chromium (18-21%) and iron (18.5-4%) in addition to relative higher contents of niobium, molybdenum, titanium, aluminum and carbon (Ref 1). Because of the excellent combination of alloying elements, Inconel alloy possesses superior mechanical properties such as high yield (700-1250 MPa) and ultimate tensile strengths (950-1650 MPa), good creep and rupture strengths and high resistance to fatigue and corrosion at elevated temperatures. This results in broad applicability in aerospace, nuclear, marine and chemical industries (Ref 2-4). However, these alloys have a narrow forming temperature range, more deformation resistance and complex microstructures (Ref 5-8). Thus, an extensive investigation on the high temperature flow behavior of Inconel alloys is very important.

Understanding deformation behavior is a key requirement to optimize process parameters for improving the material pro-

cessing conditions and conforming safe performance during forming and machining. The critical review paper by Lin and Chen (Ref 6) provides the summary of constitutive models and divided into three categories: (1) phenomenological constitutive model (2) physical-based constitutive model and (3) artificial neural network (ANN) model. Phenomenological constitutive models are based on the viscoplastic theory where several variables are aimed at stimulating the processing parameters by work hardening, thermal softening as well as strain rate softening. Cowper and Symonds (Ref 7) developed the Cowper and Symonds model to describe the true stress in terms of uniaxial effective plastic strain and strain rate. Johnson and Cook (Ref 8) derived the Johnson Cook (JC) model to relate flow stress and strain, temperature and strain rate. This model reflects only individual effect of processing parameters, but it fails to define the material properties at high strain rate and elevated temperatures (Ref 8, 9). The coupled effect of processing parameters has been considered by researcher in modified original JC model for IC10 and Al-Zn-Mg alloy (Ref 9, 10). Further, Lin et al. (Ref 11) used m-JC model for tensile flow behavior of typical high-strength steel alloy for quasi-static strain rates at high temperature range (1123-1373 K).

Physical-based constitutive model is based on the micro-mechanism of crystal plastic deformation. These models are related to principles of thermal activation energy, dislocation evolution mechanisms and dislocation interaction to predict the material flow behavior (Ref 6). Zerilli and Armstrong (ZA) model (Ref 12) is more popular physical-based model because of integral response of processing parameters, such as strain rate and temperature. But, the flow predicted using this model gives imprecise results at higher temperature (> 0.6 of melting temperature of the alloy) and lower strain rates (Ref 13). Samantaray et al. (Ref 14) formulated the modified ZA (m-ZA) model by integrating strain and temperature, strain rate and temperature responses and neglecting the athermal part to

Gauri Mahalle, Nitin Kotkunde, Amit Kumar Gupta, and **R. Sujith**, Department of Mechanical Engineering, BITS Pilani Hyderabad Campus, Hyderabad, Telangana 500078, India; **Swadesh Kumar Singh**, Department of Mechanical Engineering, GRIET, Hyderabad, Telangana 500072, India; and **Y.C. Lin**, School of Mechanical and Electrical Engineering, Central South University, Changsha 410083 Hunan Province, People's Republic of China. Contact e-mail: p20160415@hyderabad.bits-pilani.ac.in.

accurately predict flow behavior at elevated temperature. Further, researchers combined the JC and ZA model by including the average temperature rise to predicate the flow behavior of high-strength steel and Ti-6Al-4V alloy at elevated temperatures (Ref 11-18).

A few studies have been reported the relationships between flow stress and deformation parameters of Ni-based superalloy. Specially, Lin et al. (Ref 17, 19) developed a new phenomenological constitutive model to define deformation behavior of aged Inconel 718 superalloy over temperature range of 920-1040 °C and strain rate range 0.001-1 s^{-1}. This new model considered the viscoplastic constitutive model for work hardening, softening and dynamic recovery behavior and phenomenological constitutive models for dynamic softening stages. Li et al. (Ref 18) investigated the hot deformation characteristics of Ni-Cr-Fe-Ti alloy over temperature range of 880-1030 °C with strain rates of 0.01-10 s^{-1} to establish the dynamic model (DMM) and processing map.

After a thorough literature review, it is noticed that no open literature is available on the comparative study among the popular phenomenological and physical-based models together for Inconel 718 alloy over a wide range of temperatures, strains and quasi-static strain rates. Hence, the main objective of this paper is to understand the microstructure characteristics and comparative analysis of different constitutive models, mainly modified Cowper Symonds (m-CS), modified Johnson Cook (m-JC), modified Zerilli–Armstrong (m-ZA) and integrated JC-ZA model to predicate the flow behavior of Inconel 718 alloy over a wide range of temperatures and strain rates.

2. Materials and Experimental Details

Commercially available hot-rolled Inconel 718 alloy sheet with 1 mm thickness is used in hot tensile tests. The Inconel 718 alloy chemical composition is mentioned in Table 1. The dimensions of flat tensile test specimens were designed according to ASTM E08/E8 M-11 sub-sized specimens. Tensile test specimens were prepared using wire cut electric discharge machining (EDM) process. The samples were first heated to their deformation temperature at 20 °C/min, where the heat preservation time is 9-10 min in order to ensure a uniform temperature prior to loading, as shown in Fig. 1. Two-zone split heating cylindrical furnace was used for heating with contact-type extensometer, as shown in Fig. 2. Then, quasi-static hot tensile test was conducted at particular temperature and tested specimens are allowed to air cool to room temperature (RT). Tensile experiments were performed from RT to 973 K at an interval of 100 K over a wide range of slow strain rates from 0.0001, 0.001, 0.01 and 0.1 s^{-1}. Three samples were tested in each test setting, and average values were reported.

For microscopic study, the as-received sheet sample is grounded on progressively finer grades of silicon carbide impregnated with emery paper, using sufficient amount of water as a lubricant. Subsequently, the grounded samples have been polished using 5-μm diamond solution. Finally, using 1-μm diamond solution as the lubricant, a perfect mirror-like finish of the specimen has been achieved. The polished and etched surface of sample is observed under an optical microscope and photographed using standard bright-field illumination technique. Furthermore, the fractured surface of fully deformed tensile test samples is examined using a scanning electron microscope (SEM) of Hitachi, S-3400N accelerating voltage 15 kV. The observed samples are sectioned parallel to the fracture surface, as shown in Fig. 3(a). The fracture surfaces are observed with different magnifications to conclude macroscopic fracture mode and to concurrently characterize the intrinsic features on tensile fracture surface during uniaxial tensile deformation. Electron backscattered diffraction (EBSD) analysis has been studied using an orientation imaging microscopy (OIM) attachment to a field-emission scanning electron microscope (FE-SEM) operated at 20 kV. The specimen location is chosen near to deformation zone as shown in Fig. 3(b).

3. Results and Discussions

3.1 Tensile Flow Behavior

Figure 4(a) and (b) shows representative flow stress behavior at strain rate of 0.0001 and 0.01 s^{-1} with variation of temperatures in rolling direction of a sheet. It can be seen in Fig. 4(a) and (b) that temperature has significant influence on flow stress behavior. As expected, flow stress decreases at
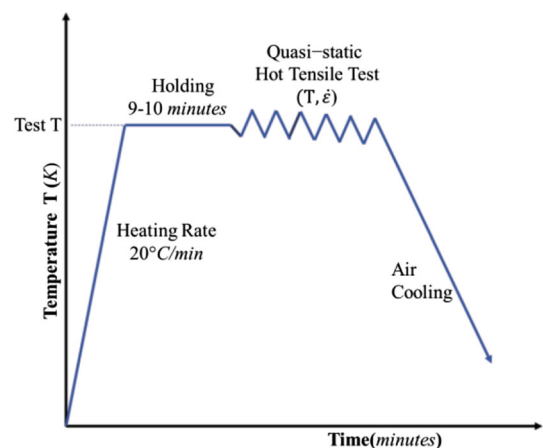

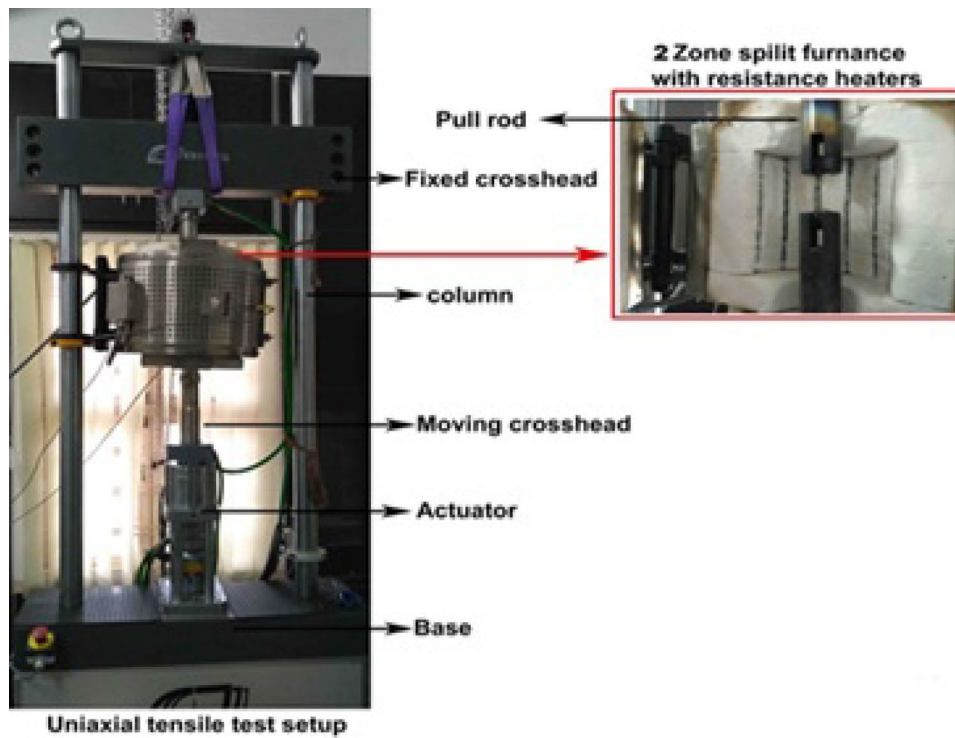Fig. 1 Experimental procedure followed quasi-static hot tensile test

Table 1 Chemical composition of Inconel 718 alloy (wt.%)

Element	Ni	Cr	Fe	Nb	Mo	Ti	Al	Mn	Si	Others
For IN718, wt.%	51.463	18.279	20.441	5.012	2.871	1.092	0.561	0.062	0.051	0.169

Other elements: each $\leq$ 0.05% and total $\leq$ 0.17%

Fig. 2 Schematic diagram of UTM of 50 kN capacity with two-zone split heating furnace
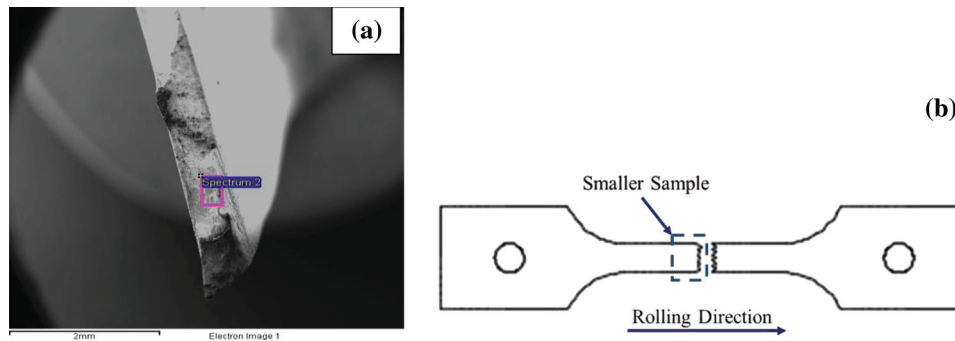

Fig. 3 (a) Fractography and (b) EBSD sample location of deformed test specimen

increasing temperature. Initially, flow stress is sharply increasing with the rise of small strain (up to 0.05), then subsequent slow increasing in the flow stress till ultimate tensile strength ($_{uts}$). The sharp increase in tensile strength is because of uniform macroscopic deformation. This uniform deformation is due to mobility of dislocation during initial stage of deformation. Usually deformation progresses with first uniform deformation, then necking either diffuse or localized and finally metal fracture (Ref 20). For all temperatures, work hardening is the predominant phenomenon observed, followed by sudden failure at strain range of 0.55-0.75. The thermal softening effect is very minimal in all cases for Inconel 718 in the tested temperature range (300-973 K).

Figure 4(c) and (d) shows representative true stress–strain graphs at particular test temperature with different strain rates. At RT, material shows strain dependence and yield strength decreases at about 506 MPa at the strain rate of 0.01 s^{-1} to 450 MPa at strain rate of 0.0001 s^{-1} (Table 2). Table 2 gives average material properties of Inconel 718 alloy at different test temperatures. The tensile strength parameters (σ_{ys} and σ_{uts}) and % elongation values decrease and increase, respectively, with increase in temperature. The reduction in yield strength is observed approx. 31% (From 506 to 345 MPa), and ultimate strength by approx. 19.8% (from 952 to 754 MPa), with improvement in % elongation from 41.8 to 54.6% from RT to 973 K. Similar observation is reported by Iturbe et al. (Ref 19) that the mechanical properties of Inconel 718 alloy decrease by an avg. of 30% until temperature exceed approx. to 973 K.

From Fig. 4(a), (b), (c) and (d), noticeable observation at lower strain rate is serrated yielding phenomenon reported over the temperature range 673-973 K for all strain rate. Serration behavior is specially described by the Portevin–Le Chatelier effect or dynamic strain ageing (DSA). According to the classification of Rodriguez, the serrations type A, B and C are generally observed in metal (Ref 21). An abrupt rise in flow stress followed by a drop-in value below mean level in stress–strain curve is characterized as type A serration, usually occurs in low-temperature range (< 673 K). The oscillation about
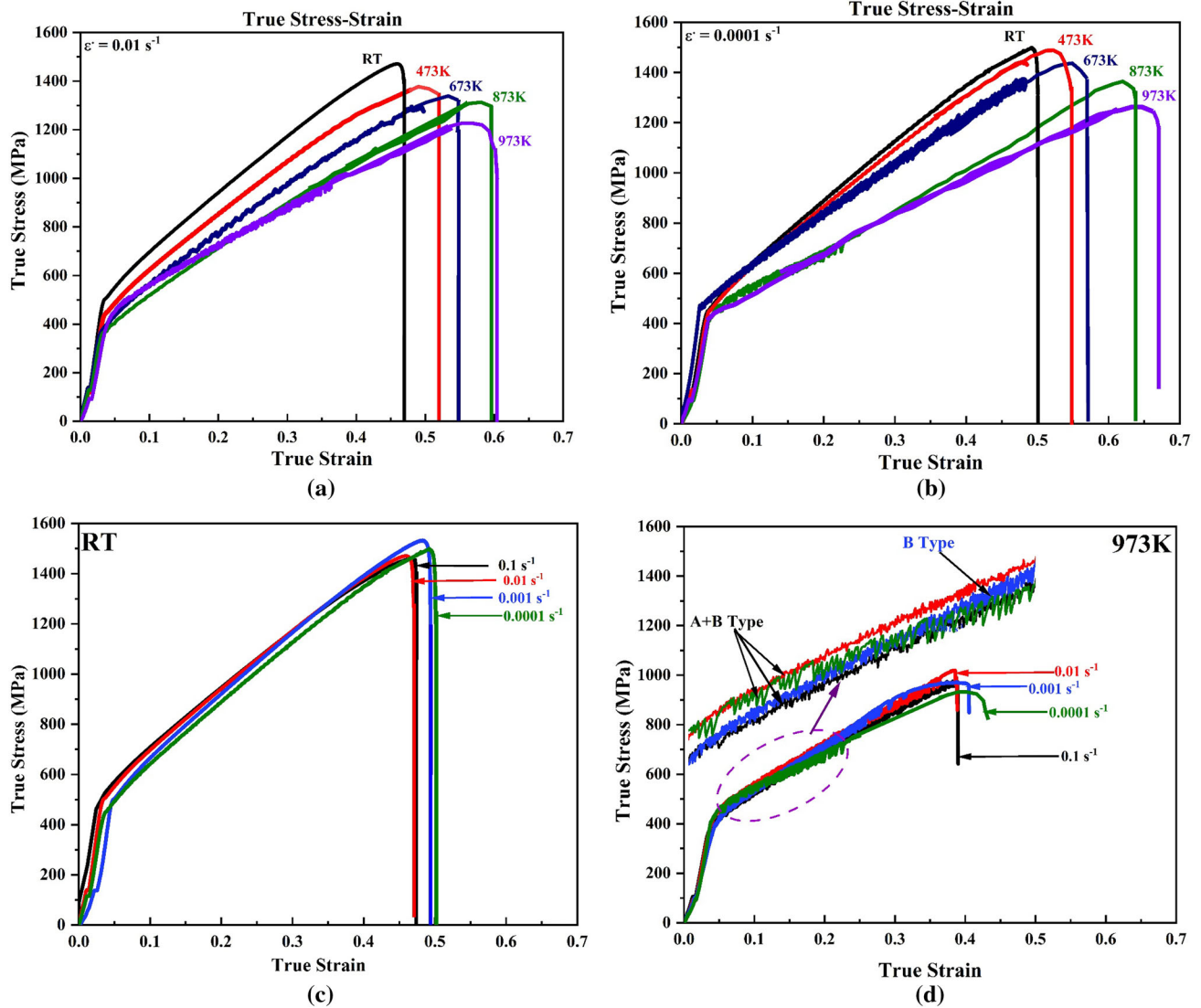
Fig. 4 Representative true stress–strain curve of Inconel 718 alloy, at various test temperatures with strain rates of (a) 0.01 s^{-1}, (b) 0.0001 s^{-1}, (c) at RT and (d) at 973 K, with various strain rates

Table 2 Average material properties of Inconel 718 alloy at different test temperatures

Temperature, K	σ_{ys}, MPa	σ_{uts}, MPa	Percent elongation, %
RT	505.64 ± 6%	951.92 ± 10%	41.97 ± 0.6
373 K	486.30 ± 5%	873.52 ± 6%	44.20 ± 0.6
473 K	443.91 ± 3%	863.58 ± 5%	47.75 ± 0.5
573 K	424.20 ± 5%	844.40 ± 4%	48.16 ± 0.5
673 K	394.66 ± 4%	819.73 ± 6%	49.22 ± 0.7
773 K	370.83 ± 6%	781.33 ± 8%	51.91 ± 0.4
873 K	358.57 ± 4%	762.14 ± 6%	53.62 ± 0.4
973 K	343.58 ± 5%	753.22 ± 6%	54.6%± 0.7

mean level in stress–strain curve is characterized as type B, usually develops prolongation from type A with temperature range (< 1023 K). These are considered as locking serrations as stress level fluctuates to mean flow stress level. As yield stress drops below the general level of mean flow stress level,

flow is characterized as the type C. It is considered unlocking serration of dislocation by intermetallic present in the alloy. The serration observed in Inconel 718 is mainly a combination of type A and B at lower temperatures, while type C at higher temperatures (> 1023 K) (Ref 22). The fluctuation of flow

stress is because of rapid DRX, where the former process ends before latter one starts (Ref 23). Similar observations regarding the nature of serration in these temperature ranges have been reported in the literature (Ref 24). Another way to confirm the DSA phenomena is strain rate sensitivity (m) parameter (Ref 25). The dependence of flow stress on strain rate measured by strain rate sensitivity (m). It is experimentally determined by comparing the stress levels at the same strain of two tensile tests at different strain rates at a particular temperature. The m parameter is calculated based on the modified Hollomon equation as (Ref 26),

$$m = \frac{\dot{\varepsilon} d\sigma}{\sigma d\dot{\varepsilon}} = \frac{\partial(\ln \sigma)}{\partial(\ln \dot{\varepsilon})} \qquad \text{(Eq 1)}$$

Table 3 represents the m value at different temperatures. The negative value of m (Table 3) confirms the claim of PLC or DSA effect in an Inconel 718 alloy from 473 to 973 K for all the strain rates.

3.2 Constitutive Modeling

Four constitutive models, namely m-CS, m-JC, m-ZA and integrated JC-ZA model, have been developed considering the coupled effect of strain, strain rate and temperature for prediction of flow stress behavior of Inconel 718 alloy.

3.2.1 Modified Cowper–Symonds (m-CS) Model. Cowper and Symonds (CS) developed a model to describe true stress in terms of uniaxial effective plastic strain (ε) and strain rate ($\dot{\varepsilon}$) (Ref 7). The flow stress for isothermal condition in CS model is formulated as:

$$\sigma_y(\varepsilon, \dot{\varepsilon}) = K\left[\varepsilon + \left(\frac{E}{K}\right)^{\frac{1}{(n-1)}}\right]^n \left[1 + \left(\frac{\dot{\varepsilon}}{C}\right)^{\frac{1}{p}}\right], \qquad \text{(Eq 2)}$$

where σ is flow stress in high-velocity testing condition and strain sensitive parameters (C & p) and hardening parameters (K & n) are evaluated by fitting stress–strain data (between yield strength and ultimate strength) at different strain rates (Ref 27, 28). The effect of strain and strain rate are combined in modified CS (m-CS) as (Ref 28),

$$\sigma_y(\varepsilon, \dot{\varepsilon}) = \sigma_y^s(\varepsilon)\left[1 + \left(\frac{\dot{\varepsilon}}{C}\right)^{\frac{1}{p}}\right] f(\varepsilon), \qquad \text{(Eq 3)}$$

where $f(\varepsilon)$ reflects the effect on strain rate sensitivity by strain and $\frac{\sigma_y(\varepsilon, \dot{\varepsilon})}{\sigma_y^s(\varepsilon)}$ defines coefficient of strain rate. Values of material constants (Table 4) are calculated as per the procedure followed by Tian et al. (Ref 28). Equation for m-CS model for Inconel 718 alloy is

$$\sigma = \left(430.06 + 3.2325 * 10^3 \varepsilon^{0.9936}\right)\left(1 + 0.0078 \ln\frac{\dot{\varepsilon}}{0.01}\right)$$
$$\times \left[1 - \frac{T - 298}{1302}\right]^{1.6221}$$
$$\text{(Eq 4)}$$

3.2.2 Modified Johnson Cook (m-JC) Model. Original JC model reflects only individual effect of processing parameters, but it fails to define the material properties at high strain rates and elevated temperatures (Ref 8, 9). A modification has been proposed in original model to resolve this problem, in which strain, temperature and strain rate couple effect are considered. Mathematical expression for m-JC model is (Ref 29),

$$\sigma = \left(A_1 + B_1\varepsilon + B_2\varepsilon^2\right)\left(1 + C_1 \ln\frac{\dot{\varepsilon}}{\dot{\varepsilon}_{\text{ref}}}\right)$$
$$\times \exp\left[\left(\lambda_1 + \lambda_2 \ln\frac{\dot{\varepsilon}}{\dot{\varepsilon}_{\text{ref}}}\right)(T - T_{\text{ref}})\right] \qquad \text{(Eq 5)}$$

where A_1, B_1, B_2, λ_1, λ_2 are material constants added in Eq 5. m-JC model captures the coupled effect of strain rate and temperature, and strain and temperature which is not captured by original JC model. The values of material constants are calculated according to the procedure mentioned by Lin et al. (Ref 11). Thus, all of the material constants of the m-JC model are calculated and précised in Table 5. Equation for m-JC model for Inconel 718 alloy is

$$\sigma = \left(444.95 + 3180.3\varepsilon - 187.29_2\varepsilon^2\right)\left(1 + 0.0036_1 \ln\frac{\dot{\varepsilon}}{0.01}\right)$$
$$\times \exp\left[\left(-0.0002 + 0.0013 \ln\frac{\dot{\varepsilon}}{(0.01)}\right)(T - 298)\right]$$
$$\text{(Eq 6)}$$

3.2.3 Modified Zerilli–Armstrong (m-ZA) Model. Zerilli and Armstrong (Ref 28, 30) suggested constitutive equation based on thermal activation by dislocation. The m-ZA (Ref 14) proposed as

$$\sigma = (C_1 + C_2\varepsilon^n)\exp\{(-C_3 + C_4\varepsilon)(T - T_{\text{ref}})$$
$$+ \left[C_5 + C_6(T - T_{\text{ref}})\ln\left(\frac{\dot{\varepsilon}}{\dot{\varepsilon}_{\text{ref}}}\right)\right]\} \qquad \text{(Eq 7)}$$

where C_1 is the yield strength of Inconel 718 alloy at reference strain rate ($\dot{\varepsilon}_{\text{ref}} = 0.01 \text{ s}^{-1}$) and temperature (298 K), C_2 is the strain hardening coefficient, and n, C_3, C_4, C_5, C_6 are material

Table 4 Material constants for m-CS constitutive model

Temperature, K	K, MPa	n	C	P	R-square
RT	438.69	0.435	6.21	7.02	0.991
373 K	402.58	0.379	7.52	9.653	0.983
473 K	395.29	0.375	9.39	14.20	0.969
573 K	365.96	0. 367	9.66	15.65	0.948
673 K	325.18	0.264	10.93	16.14	0.940
773 K	321.54	0.152	13.52	11.55	0.926
873 K	308.06	0.157	15.56	8.097	0.923
973 K	292.63	0.255	16.35	9.577	0.945

Table 3 Strain rate sensitivity (m) values for different temperatures

Temperature, K	RT	373 K	473 K	573 K	673 K	773 K	873 K	973 K
Strain rate sensitivity (m)	0.0053	0.0049	− 0.0186	− 0.108	− 0.121	− 0.179	− 0.281	− 0.12

constants which incorporates influence of temperature, coupled effect of temperature and strain, effect of strain rate and coupled effect of strain rate and temperature, respectively. The material constants (Table 6) are calculated using procedure discussed by Samantaray et al. (Ref 31). Smaller value of C_3 and C_5 indicates lesser effect of temperature on flow behavior and strain rate sensitivity on Inconel 718 alloy. Equation for m-ZA is given as,

$$\sigma = \left(260 + 1452.5\varepsilon^{0.884}\right)\exp\left(-\left(7.7465*10^{-4} - 7.533*10^{-4}\varepsilon\right)\right.$$
$$\left. \times (T - 298) + \left(0.0173 - 6.8605*10^{-5}(T - 298)\ln\left(\frac{\dot{\varepsilon}}{0.01}\right)\right)\right)$$
(Eq 8)

3.2.4 Integrated JC-ZA Model. Nadai (Ref 32) first proposed integrated JC-ZA model combining strain hardening term from JC model and strain rate and temperature coupled term from ZA model to take advantage of both models. The integrated JC-ZA model is mathematically expressed as:

$$\sigma = (A + B\varepsilon^n)\left(-C_3 T + C_4 T \ln\frac{\dot{\varepsilon}}{\dot{\varepsilon}_{\text{ref}}}\right)$$
(Eq 9)

where A, B, C_3, C_4 and n are material constants, $\dot{\varepsilon}_{\text{ref}} = 0.01 \text{ s}^{-1}$ considered. Considering the effect of plastic deformation energy, Eq. 9 can be modified as (Ref 33),

$$\sigma = (A + B\varepsilon^n)\left[C_3(T + \Delta T) + C_4(T + \Delta T)\ln\left(\frac{\dot{\varepsilon}}{\dot{\varepsilon}_{\text{ref}}}\right)\right]$$
(Eq 10)

where ΔT is measured averaged rise in temperature due to deformation heat to overcome the substantial plastic work (Ref 33). Further, a new integrate model is proposed by Che et al. (Ref 32), considering first term consists of Hall–Petch relation (effect of grain size on σ_y and combined effect of strain rate and strain) and second term of m-ZA (combined effect of strain and temperature and of temperature and strain rate), mathematically expressed as:

$$\sigma = \left(\left(a + \frac{k}{\sqrt{d}}\right) + B\left(1 - \frac{\ln\dot{\varepsilon}}{\ln D_0}\right)^{n_2}\varepsilon^{n_1}\right)$$
$$\times \exp\left\{-(C_3 + C_4\varepsilon)(T - T_{\text{ref}}) + C_5 + C_6(T - T_{\text{ref}})\ln\left(\frac{\dot{\varepsilon}}{\dot{\varepsilon}_{\text{ref}}}\right)\right\}$$
(Eq 11)

where $\left(a + \frac{k}{\sqrt{d}}\right)$ is Hall–Petch relation, D_0 is deformation rate (arbitrarily selected as 10^6 upper bound strain rate) and n_2, n_1, C_3, C_4, C_5 and C_5 have same definition as original m-JC and m-ZA model. This new integrated model increases the accuracy as it considers the effect of grain size, strain rate, strain hardening, thermal softening and combined effects of strain, strain rate and temperature. The material constants are calculated using procedure stated by Che et al. (Ref 32) and listed in (Table 7). The equation for JC-ZA is given as

$$\sigma = \left(260 + 1452.5\varepsilon^{0.884}\right)$$
$$\times \exp\left(-\left(7.7465*10^{-4} - 7.533*10^{-4}\varepsilon\right)(T - 298)\right.$$
$$\left. + \left(0.0173 - 6.8605*10^{-5}(T - 298)\ln\left(\frac{\dot{\varepsilon}}{0.01}\right)\right)\right)$$
(Eq 12)

3.3 Constitutive Modeling Comparison

Capability of m-CS, m-JC, m-ZA and JC-ZA models is evaluated by comparing the predicted flow stress with experimental data. Figure 5(a), (b), (c) and (d) represents comparative flow stress behavior at different temperatures and strain rates for m-CS, m-JC, m-ZA and JC-ZA model, respectively. Figure 5(a) indicates a linear relationship between coefficient of strain rate $\left(\frac{\sigma_y(\varepsilon,\dot{\varepsilon})}{\sigma_y^s(\varepsilon)}\right)$ and strain at test temperature. But, it is observed that there are some nonconformities between experimentally measured and predicted values of flow stress at lowest strain rate of 0.0001 s^{-1} for m-CS model. In the case of m-JC model (Fig. 5b), the prediction is better than m-CS model except at RT condition. Subsequently, m-ZA and JC-ZA models show good correlation between predicted and experimentally measured flow stress.

Generally, suitability of constitutive models has been compared by various statistical parameters like correlation coefficient (R). Table 8 provides comparison of statistical parameters for all considered models. It can be seen in Table 8 that m-CS model shows poor correlation coefficient $(R = 0.9324)$ among all other models. All other models show

Table 5 Material constants for m-JC constitutive model

A_1, MPa	B_1	B_2	C_1	λ_1	λ_2
444.95	3180.3	− 187.29	0.0036	− 0.0002	0.0013

Table 6 Material constants for m-ZA constitutive model

C_1, MPa	C_2, MPa	C_3	C_4	C_5	C_6	n
260	1.453e3	7.747e(− 4)	− 7.533e(− 4)	0.0173	− 6.861e(− 5)	0.884

Table 7 Material constants for integrated JC-ZA constitutive model

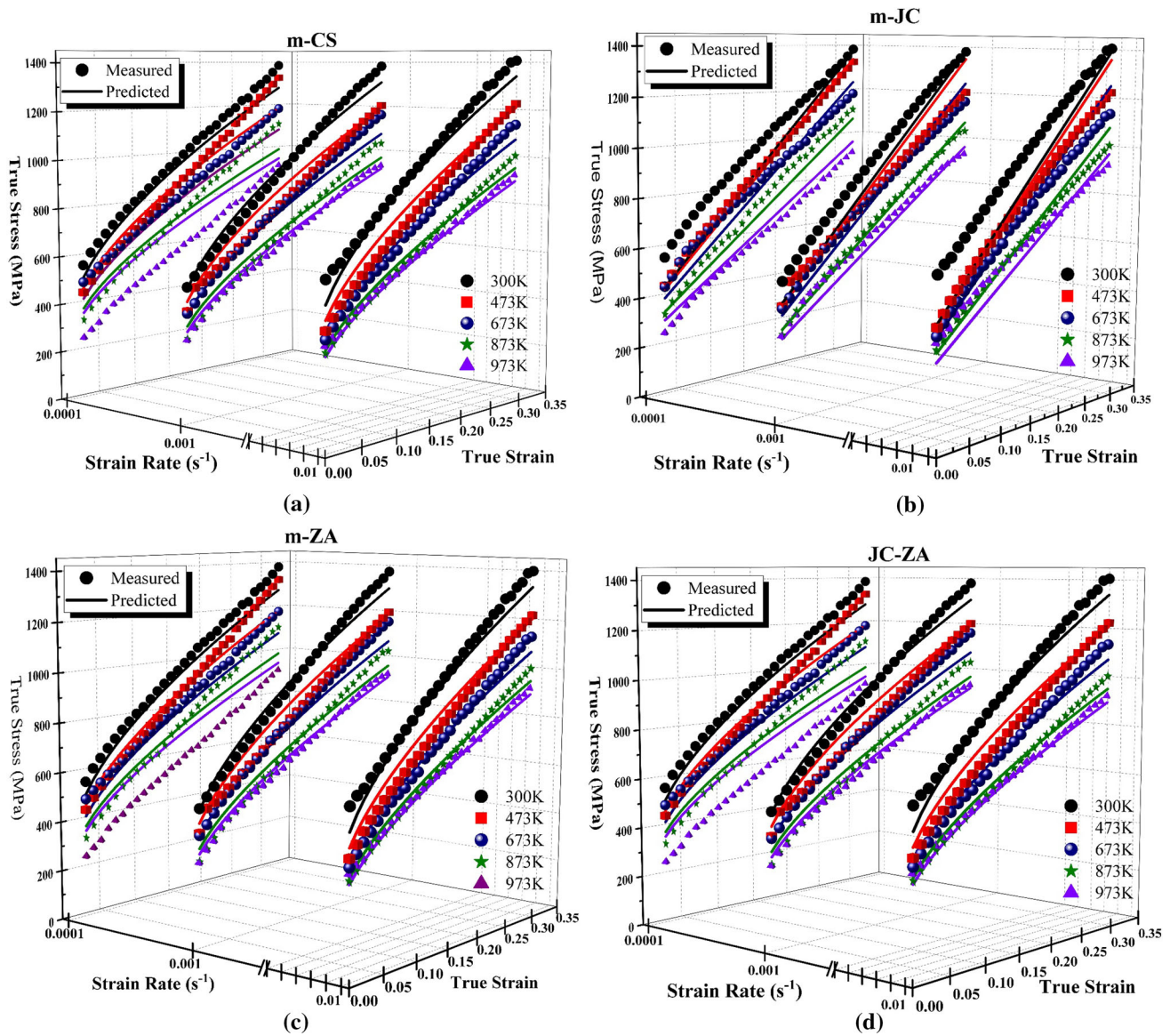| a, MPa	k, MPa	B	n_1	n_2	C_3	C_4	C_5	C_6
536.06	901	1980	− 1.1764	1.022	7.166e(− 4)	− 6.338e(4)	− 9.350e(− 4)	− 4.304e(−5)

Fig. 5 Plot showing comparison between experimentally measured and predicted flow stress for strain rates: 0.01 s^{-1}, 0.001 s^{-1} and 0.0001 s^{-1} by (a) m-CS model (b) m-JC model (c) m-ZA model (d) JC-ZA model

Table 8 Comparison between m-CS, m-JC, m-ZA and integrated JC-ZA model

Comparative parameters	m-CS	m-JC	m-ZA	JC-ZA
R	0.9324	0.9637	0.9641	0.9873
Δ (%)	7.53	8.46	11.19	2.44
s (%)	13.32	5.49	5.48	4.08

better and comparable correlation coefficient, as *R* value is above 0.96. Since correlation coefficient is a biased parameter and value may be biased toward higher or lower values (Ref 31, 34, 35), other statistical parameters such as average absolute error (Δ) and its standard deviation (s) are considered for comparison. Table 8 shows average values of average absolute error (Δ) and its standard deviation (s) for all the models. It can be observed that absolute error value and its standard deviation for integrated JC-ZA model are less, compared to other models.

The highest error value is found for m-ZA model of 11.19%. Based on all the statistical parameters comparison, JC-ZA model shows highest correlation accuracy with least average absolute error and standard deviation than other models.

The above comparative discussion is based on average absolute error (Δ) and its standard deviation (s). It is worth to analyze the performance of model based on average absolute error (Δ) at different temperatures and strain rates. Therefore, average absolute error (Δ) values have been calculated for different temperatures and different strain rates as shown in Fig. 6(a), (b) and (c). It is also found from Fig. 6 that m-CS prediction is less accurate than other models for all the temperatures and strain rates. The average error percentage is substantially high in higher strain rates (0.01 s^{-1}) than the lower strain rates. The Δ = 19% is reported at RT and 0.01 s^{-1}. Furthermore, m-JC and m-ZA show consistent results in case of all the temperatures and strain rates. Since, m-JC is a phenomenological-based model, i.e., the model does not consider the physical aspects of materials like dislocation
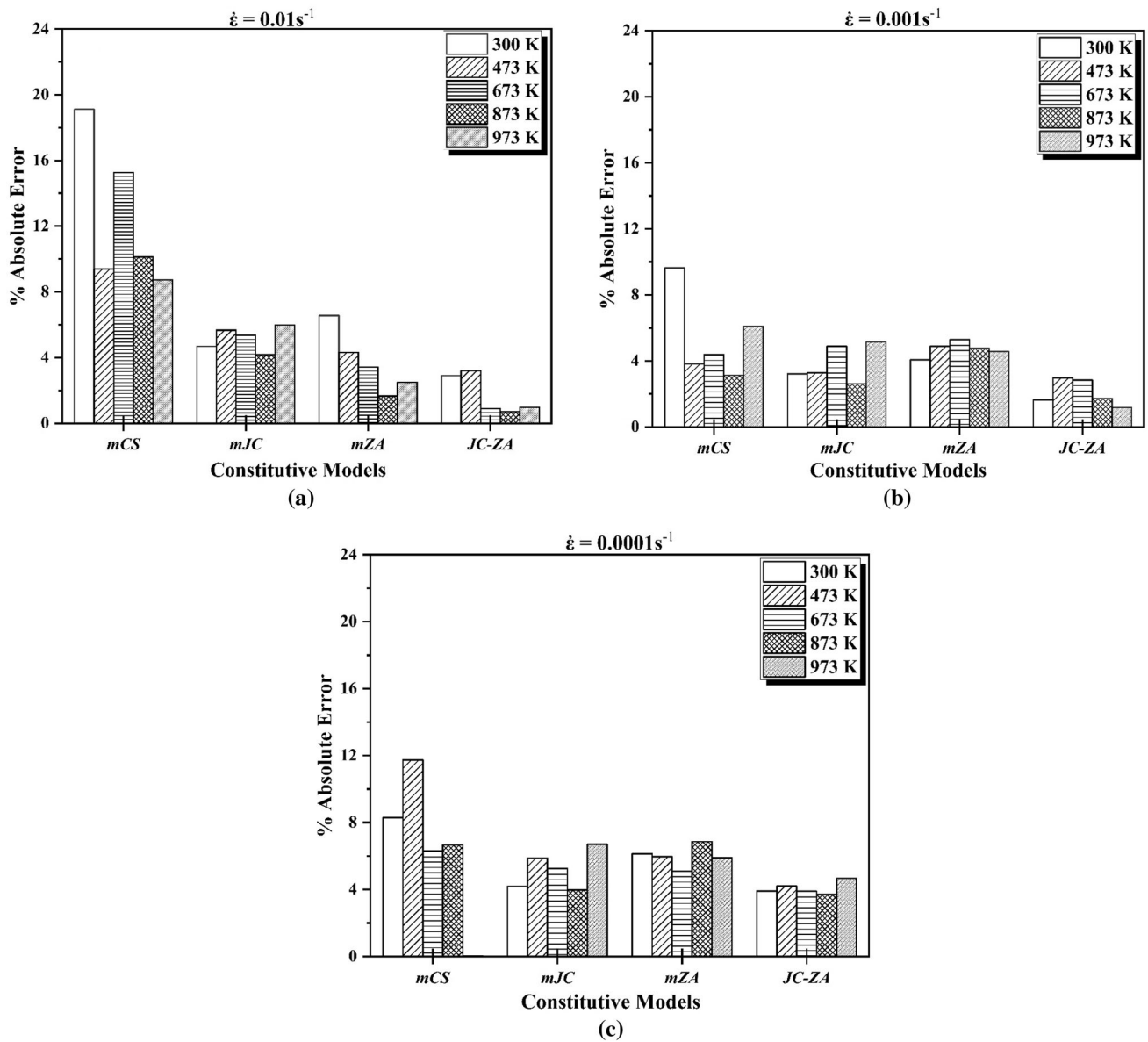
Fig. 6 Variation of % absolute error for each model with individual temperature for Inconel 718 at strain rates of (a) 0.01 s^{-1}, (b) 0.001 s^{-1} and (c) 0.0001 s^{-1}
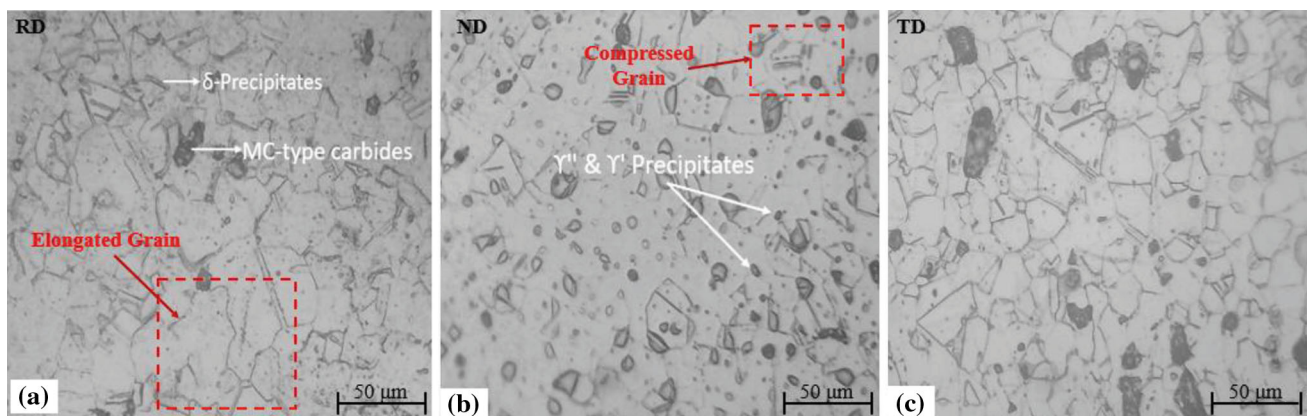

Fig. 7 Optical micrographs showing the key micro-constituents in Inconel 718 alloy at 500X magnification (a) RD (b) ND (c) TD
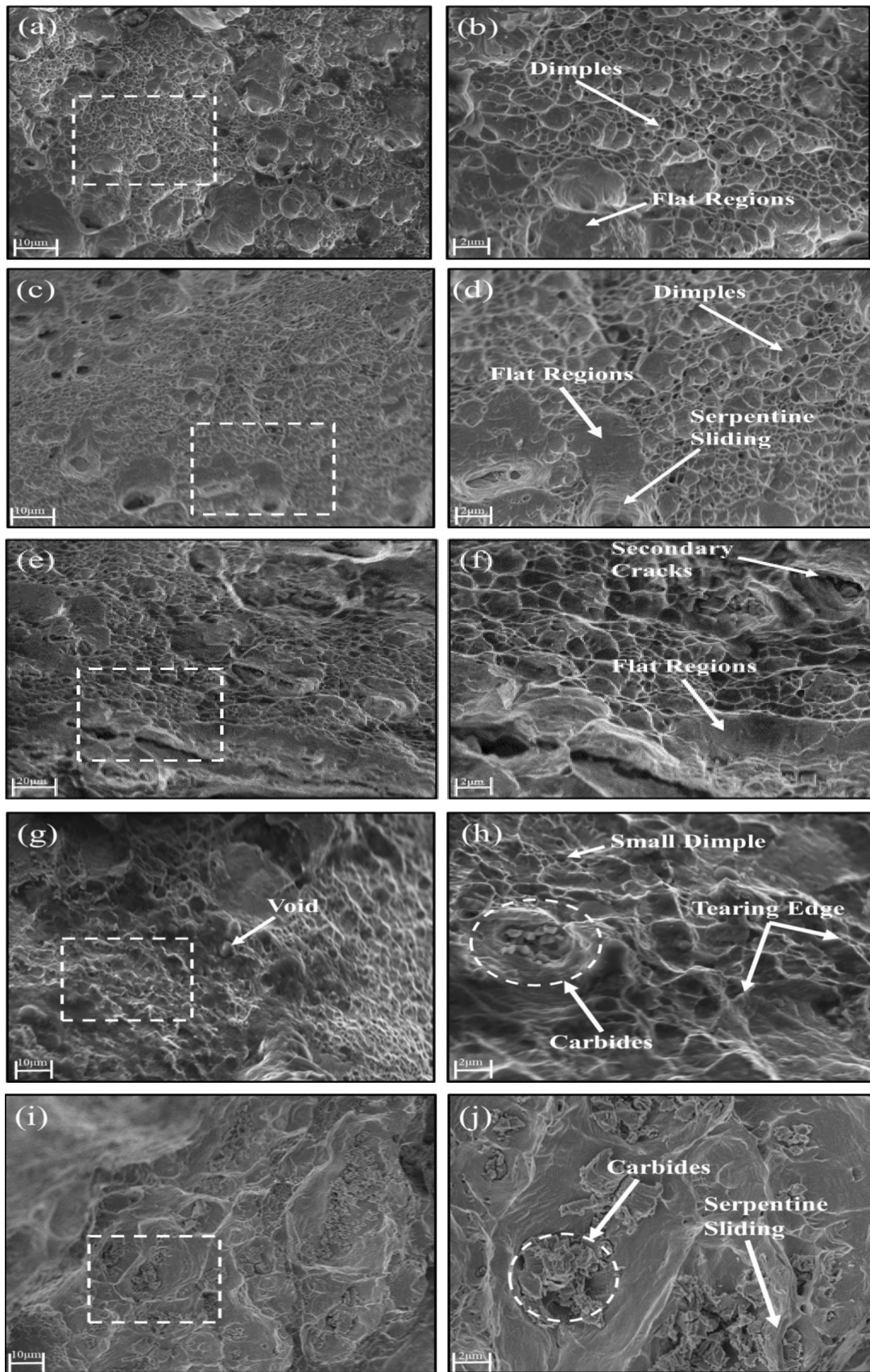
Fig. 8 Fracture surface of Inconel 718 alloy at (a-b) RT (c-d) 473 K (e-f) 673 K (g-h) 873 K (i-j) 973 K at strain rates of 0.001 s^{-1}
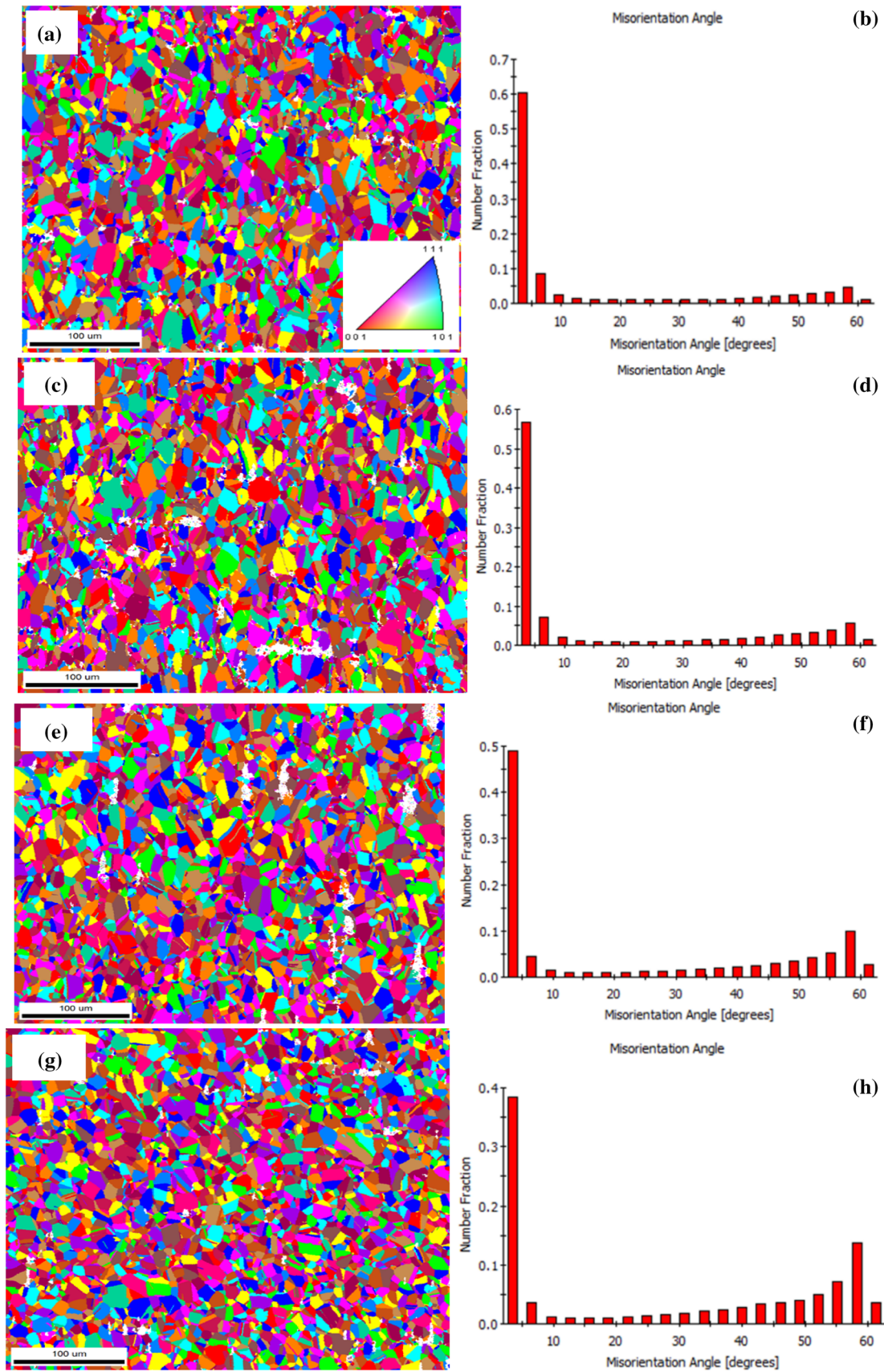
Fig. 9 Orientation imaging micrograph and misorientation angle distribution at different temperatures (a-b) *RT* (c-d) 673 K (e-f) 873 K (g-h) 973 K at strain rates of 0.001 s^{-1}

movement, kinetics of slips and various thermodynamic aspects while predicting the flow stress, whereas m-ZA is a physical-based model. Thus, m-ZA model is considered over m-JC model for flow stress prediction. Furthermore, integrated JC-ZA model shows least error values in all the temperatures and strain rates and also cover physical aspects. Integrated JC-ZA model considers the strain hardening with Hall–Petch relation to describe the flow stresses at equivalent strain value. Moreover, the concept of thermal softening along with the effect of grain size is accountable for the thermal activation energy along with mobile dislocation interactions mechanisms at higher strain. Therefore, integrated JC-ZA model is best suitable for flow stress prediction of Inconel 718 alloy over the wide range of temperatures, strain and strain rates.

3.4 Microstructure Characteristics

The metallographic observations are obtained by metallurgical microscopy with a difference in morphology in rolling (RD), diagonal to rolling (ND) and transverse (TD) directions of the metal sheet as shown in Fig. 7. As-received specimen is observed mostly fine with elongated and compressed grain size in ND and RD directional planes with considerable carbide stringers in austenitic matrix consisting of fine equiaxed grains. The presence of initial carbide is probably due to solidification procedure and influence parameters like solidification time, Nb/C ratio of alloy and cooling rate. Mitchell (Ref 36) reported that the presence of carbide at early stage of solidification was the result of final solidification of liquid alloy, which remains at eutectic instead of isolated primary carbide.

Figure 8(a), (b), (c), (d), (e), (f), (g), (h), (i) and (j) shows sectional fracture surface of post-tensile specimen of Inconel 718 at different temperatures. The sectional fracture surface is covered with plenty of dimples-serpentine sliding characteristics appearing on dimple walls, flat regions and tearing edges in Fig. 8(a), (b), (c), (d), (e) and (f). Formed carbides in Inconel 718 with dimples and tearing edges are observed in Fig. 8(g), (h), (i) and (j). These observations clearly indicate that the fracture mode of Inconel 718 at various temperatures is mixture of ductile and brittle transgranular fracture with dimples seen on main fracture feature. The size of cell-like structure and dimple are fine in nature from RT to 673 K, while the dimple size appears to increase drastically at 973 K. Similarly, fracture surfaces show large number of voids at RT which tends to decrease with increase in temperature. Nucleation and micro-voids growth are the main fracture phenomena observed in Inconel 718 alloy. At 873 and 973 K, the number of micro-voids observed was minimal with the presence of NbC-carbides and oxides in large-sized dimples (Fig. 8g-j). The presence of carbide at 873 and 973 K indicates that the precipitating phase of Inconel 718 alloy has started. Prasad et al. (Ref 26) reported that the precipitation phase mainly includes body-centered tetragonal and FCC coherent precipitates of $\gamma''(Ni_3Al)$ and γ' (Ni_3Al), respectively. These different types of formed carbides also improve the creep strength of alloy at respective working temperature. It is observed that grains in the center of specimen are heavily deformed and evidence of slip bands is found inside the grains, up to the temperature of 973 K (Fig. 8i-j). Slip bands are usually related to strain hardening phenomena, which are main deformation mechanisms observed in the stress–strain curves at less temperature of 973 K (Fig. 8a-g). The observed

serration flow phenomenon promotes the flow localization and reduces ductility, raising the deformation temperature (Ref 22).

EBSD studies were carried out to understand the influence of temperature on microstructural evolution during dynamic recrystallization. The OIM and corresponding misorientation angle distribution of Inconel 718 alloy subjected to tensile testing at RT, 673 K, 873 K and 973 K are shown in Fig. 9(a), (b), (c), (d), (e), (f), (g) and (h). The grain size of tensile-tested sample at RT, 673 K, 873 K and 973 K samples are ~ 12.12, 12.08, 12.09 and 10.87 μm, respectively. It is interesting to observe that grain coarsening has not occurred in Inconel 718 alloy, mainly due to the pinning effect by the presence of intermetallic phases at the grain boundaries. This infers that in case of Inconel 718 alloy, dynamic recrystallization mechanism seems to start at relatively lower testing temperature and the effect is more pronounced at higher testing temperature. Generation of substructures during DRX is a thermally activated process and is enhanced at higher testing temperature (Ref 24). This contributes to increase in the frequency of DRX grains, leading to a significant increase in the average misorientation angle from ~ 14 to 28°. However, DRX seems to dominate at all the testing temperatures, and formation of these grains leads to dynamic softening and substantial decrease in the tensile strength.

4. Conclusion

This work involves hot tensile testing, microstructure characteristics and comparative evaluation of various constitutive models, namely m-CS, m-JC, m-ZA and JC-ZA for Inconel 718 alloy at wide range of temperatures and strain rates. Based on the study, following important conclusions can be drawn:

1. The tensile flow stress and strain hardening behaviors are significantly affected by test temperatures and strain rates for Inconel 718 alloy. The DSA phenomenon is reported from 673 to 973 K at all the strain rate conditions. Mainly, B and combination of A and B type of serrations are observed at different temperatures and strain rates.
2. The predictions capability of m-CS model has more deviation in terms of least correlation coefficient and higher average absolute error and standard deviation. However, all other models (m-JC, m-ZA and JC-ZA) show good agreement in terms of correlation coefficient ($R > 0.96$). Among these models, JC-ZA model shows best agreement in terms of highest correlation coefficient and least average absolute error. Besides, this model also considered physical aspects of deformation.
3. The fracture surfaces of Inconel 718 alloy at various temperatures clearly indicate a ductile–brittle fracture. Nucleation and micro-voids growth are the main fracture phenomena observed in Inconel 718 alloy. From EBSD study, dynamic recrystallization mechanism seems to start at relatively lower testing temperatures, i.e., 573 K, and effect is more pronounced at higher testing temperatures.

Future work involves integration of these developed constitutive models in the finite element analysis of various metal forming processes.

References

1. Special Metals, 'INCONEL Alloy 718', 2007, doi:SMC-066
2. R.C. Reed, *The Superalloys: Fundamentals and Applications* (Cambridge University Press, New York, 2006)
3. R.E. Schafrik, D.D. Ward, and J.R. Groh, Application of Alloy 718 in GE Aircraft Engines: Past, Present and Next Five Years, *International symposium; 5th, Superalloys; Superalloys 718, 625, 706 Var. Deriv.* Minerals, Metals, and Materials Society, (Warrendale, PA, 2001)
4. Y.C. Lin, J. Deng, Y.Q. Jiang, D.X. Wen, and G. Liu, Effects of Initial δ Phase on Hot Tensile Deformation Behaviors and Fracture Characteristics of a Typical Ni-Based Superalloy, *Mater. Sci. Eng. A*, 2014, **598**, p 251–262
5. P. Zhang, C. Hu, C. Gang Ding, Q. Zhu, and H. Yong Qin, Plastic Deformation Behavior and Processing Maps of a Ni-Based Superalloy, *Mater. Des.*, 2015, **65**, p 575–584
6. Y.C. Lin and X.M. Chen, A Critical Review of Experimental Results and Constitutive Descriptions for Metals and Alloys in Hot Working, *Mater. Des.*, 2011, **32**(4), p 1733–1759
7. M. Alves, Material Constitutive Law for Large Strains and Strain Rates, *J. Eng. Mech.*, 2000, **126**, p 215–218
8. G.R. Johnson and W.H. Cook, Fracture Characteristics of Three Metals Subjected to Various Strains, Strain Rates, Temperatures and Pressures, *Eng. Fract. Mech.*, 1985, **21**(1), p 31–48
9. G. Chen, L. Chen, G. Zhao, C. Zhang, and W. Cui, Microstructure Analysis of an Al-Zn-Mg Alloy during Porthole Die Extrusion Based on Modeling of Constitutive Equation and Dynamic Recrystallization, *J. Alloys Compd.*, 2017, **710**, p 80–91
10. H. Zhang, W. Wen, and H. Cui, Behaviors of IC10 Alloy over a Wide Range of Strain Rates and Temperatures: Experiments and Modeling, *Mater. Sci. Eng. A*, 2009, **504**, p 99–103
11. Y.C. Lin, X.M. Chen, and G. Liu, A Modified Johnson-Cook Model for Tensile Behaviors of Typical High-Strength Alloy Steel, *Mater. Sci. Eng. A*, 2010, **527**(26), p 6980–6986
12. F.J. Zerilli and R.W. Armstrong, Dislocation-Mechanics-Based Constitutive Relations for Material Dynamics Calculations, *J. Appl. Phys.*, 1987, **61**, p 1816–1825
13. W.-S. Lee and C.-Y. Liu, The Effects of Temperature and Strain Rate on the Dynamic Flow Behaviour of Different Steels, *Mater. Sci. Eng. A*, 2006, **426**(1–2), p 101–113
14. D. Samantaray, S. Mandal, U. Borah, A.K. Bhaduri, and P.V. Sivaprasad, A Thermo-Viscoplastic Constitutive Model to Predict Elevated-Temperature Flow Behaviour in a Titanium-Modified Austenitic Stainless Steel, *Mater. Sci. Eng. A*, 2009, **526**(1–2), p 1–6
15. L. Chen, G. Zhao, and J. Yu, Hot Deformation Behavior and Constitutive Modeling of Homogenized 6026 Aluminum Alloy, *Mater. Des.*, 2015, **74**, p 25–35
16. Y.C. Lin, D.X. Wen, J. Deng, G. Liu, and J. Chen, Constitutive Models for High-Temperature Flow Behaviors of a Ni-Based Superalloy, *Mater. Des.*, 2014, **47**, p 115–123
17. Y.C. Lin, K.-K. Li, H.-B. Li, J. Chen, X.-M. Chen, and D.-X. Wen, New Constitutive Model for High-Temperature Deformation Behavior of Inconel 718 Superalloy, *Mater. Des.*, 2015, **74**, p 108–118
18. B. Li, Y. Du, and Z. Peng, Investigation on the Hot Deformation Characteristics of Ni-Cr-Fe-Ti Alloy, *Vacuum*, 2018, **157**, p 299–305
19. A. Iturbe, E. Giraud, E. Hormaetxe, A. Garay, G. Germain, K. Ostolaza, and P.J. Arrazola, Mechanical Characterization and Modelling of Inconel 718 Material Behavior for Machining Process Assessment, *Mater. Sci. Eng. A*, 2017, **682**, p 441–453
20. G.E. Dieter and D. Bacon, *Mechanical Metallurgy SI*, Metric edn. (McGraw-Hill Book Company, London, 1988)
21. P. Rodriguez, Serrated Plastic Flow, *Bull. Mater. Sci.*, 1984, **6**(4), p 653–663
22. Y.C. Lin, H. Yang, Y. Xin, and C.Z. Li, Effects of Initial Microstructures on Serrated Flow Features and Fracture Mechanisms of a Nickel-Based Superalloy, *Mater. Charact.*, 2018, **144**, p 9–21
23. D. Kuhlmann-Wilsdorf, Theory of Plastic Deformation: Properties of Low Energy Dislocation Structures. Mater. Sci. Eng. A **113**, 1–41 (1989)
24. N. Nayan, N.P. Gurao, S.V.S. Narayana Murty, A.K. Jha, B. Pant, and K.M. George, Microstructure and Micro-Texture Evolution during Large Strain Deformation of Inconel Alloy IN718, *Mater. Charact.*, 2015, **110**, p 241–256
25. S.M. Hussaini, S.K. Singh, and A.K. Gupta, Formability of Austenitic Stainless Steel 316 Sheet in Dynamic Strain Aging Regime, *Acta Metall. Slovaca*, 2014, **20**(1), p 71–81
26. Y.V.R.K. Prasad, K.P. Rao, and S. Sasidhara, *Hot Working Guide—A Compendium of Processing Maps* (ASM International, 2015)
27. S.S. Panicker, H.G. Singh, S.K. Panda, and R. Dashwood, Characterization of Tensile Properties, Limiting Strains, and Deep Drawing Behavior of AA5754-H22 Sheet at Elevated Temperature, *J. Mater. Eng. Perform.*, 2015, **24**(11), p 4267–4282
28. Y. Tian, L. Huang, H. Ma, and J. Li, Establishment and Comparison of Four Constitutive Models of 5A02 Aluminium Alloy in High-Velocity Forming Process, *Mater. Des.*, 2014, **54**, p 587–597
29. N. Kotkunde, H.N. Krishnamurthy, P. Puranik, A.K. Gupta, and S.K. Singh, Microstructure Study and Constitutive Modeling of Ti-6Al-4V Alloy at Elevated Temperatures, *Mater. Des.*, 2014, **54**, p 96–103
30. D.G. Tari and M.J. Worswick, Journal of Materials Processing Technology Elevated Temperature Constitutive Behavior and Simulation of Warm Forming of AZ31B, *J. Mater. Process. Technol.*, 2015, **221**, p 40–55
31. D. Samantaray, S. Mandal, and A.K. Bhaduri, A Comparative Study on Johnson Cook, Modified Zerilli-Armstrong and Arrhenius-Type Constitutive Models to Predict Elevated Temperature Flow Behaviour in Modified 9Cr-1Mo Steel, *Comput. Mater. Sci.*, 2009, **47**, p 568–576
32. J. Che, T. Zhou, Z. Liang, J. Wu, and X. Wang, An Integrated Johnson-Cook and Zerilli-Armstrong Model for Material Flow Behavior of Ti-6Al-4V at High Strain Rate and Elevated Temperature, *J. Braz. Soc. Mech. Sci. Eng.*, 2018, **40**(253), p 1–10
33. Y.C. Lin and X.M. Chen, A Combined Johnson-Cook and Zerilli-Armstrong Model for Hot Compressed Typical High-Strength Alloy Steel, *Comput. Mater. Sci.*, 2010, **49**(3), p 628–633
34. L. Chen, G. Zhao, J. Yu, and W. Zhang, Constitutive Analysis of Homogenized 7005 Aluminum Alloy at Evaluated Temperature for Extrusion Process, *Mater. Des.*, 2015, **66**, p 129–136
35. L. Chen, G. Zhao, J. Gong, X. Chen, and M. Chen, Hot Deformation Behaviors and Processing Maps of 2024 Aluminum Alloy in As-Cast and Homogenized States, *J. Mater. Eng. Perform.*, 2015, **24**, p 5002–5012
36. A. Mitchell, The Precipitation of Primary Carbides in IN718 and Its Relation to Solidification Conditions, *Superalloys 718, 625, 706 Var. Deriv.*, 2005, **20**, p 299–310

Publisher's Note Springer Nature remains neutral with regard to jurisdictional claims in published maps and institutional affiliations.